



HAL
open science

Experimental Measurement of Enhanced and Hindered Particle Settling in Turbulent Gas-Particle Suspensions, and Geophysical Implications

Baptiste Penlou, Olivier Roche, Michael Manga, Siet van den Wildenberg

► **To cite this version:**

Baptiste Penlou, Olivier Roche, Michael Manga, Siet van den Wildenberg. Experimental Measurement of Enhanced and Hindered Particle Settling in Turbulent Gas-Particle Suspensions, and Geophysical Implications. *Journal of Geophysical Research: Solid Earth*, 2023, 128 (3), 10.1029/2022JB025809 . hal-04012883

HAL Id: hal-04012883

<https://uca.hal.science/hal-04012883v1>

Submitted on 3 Mar 2023

HAL is a multi-disciplinary open access archive for the deposit and dissemination of scientific research documents, whether they are published or not. The documents may come from teaching and research institutions in France or abroad, or from public or private research centers.

L'archive ouverte pluridisciplinaire **HAL**, est destinée au dépôt et à la diffusion de documents scientifiques de niveau recherche, publiés ou non, émanant des établissements d'enseignement et de recherche français ou étrangers, des laboratoires publics ou privés.

1 **Experimental measurement of enhanced and hindered**
2 **particle settling in turbulent gas-particle suspensions,**
3 **and geophysical implications**

4 **Baptiste Penlou¹, Olivier Roche¹, Michael Manga², Siet van den Wildenberg^{1,3}**

5 ¹Université Clermont Auvergne, CNRS, IRD, OPGC, Laboratoire Magmas et Volcans, Clermont-Ferrand,
6 F-63000, France

7 ²Department of Earth and Planetary Science, University of California, Berkeley, CA, USA

8 ³Université Clermont Auvergne, CNRS/IN2P3, Laboratoire de Physique de Clermont, Clermont-Ferrand,
9 F-63000, France

10 **Key Points:**

- 11 • We investigate the relationship between particle concentration and particle set-
12 tling velocity in turbulent air-particle mixtures.
- 13 • We demonstrate an interplay between hindered settling and cluster-induced en-
14 hanced settling, depending on the Stokes number.
- 15 • Clustering of 78 μm particles increases mean settling velocity, while 467 μm par-
16 ticles experience hindered settling.

Corresponding author: Siet van den Wildenberg, siet.van.den.wildenberg@uca.fr

Abstract

The dynamics of geophysical dilute turbulent gas-particles mixtures depends to a large extent on particle concentration, which in turn depends predominantly on the particle settling velocity. We experimentally investigate air-particle mixtures contained in a vertical pipe in which the velocity of an ascending air flux matches the settling velocity of glass particles. To obtain local particle concentrations in these mixtures, we use acoustic probing and air pressure measurements and show that these independent techniques yield similar results for a range of particle sizes and particle concentrations. Moreover, we find that in suspensions of small particles ($78\ \mu\text{m}$) the settling velocity increases with the local particle concentration due to the formation of particle clusters. These clusters settle with a velocity that is four times faster than the terminal settling velocity of single particles, and they double settling speeds of the suspensions. In contrast, in suspensions of larger particles ($467\ \mu\text{m}$) the settling velocity decreases with increasing particle concentration. Although particle clusters are still present in this case, the settling velocity is decreased by 30%, which is captured by a hindered settling model. These results suggest an interplay between hindered settling and cluster-induced enhanced settling, which in our experiments occur respectively at Stokes number $O(100)$ and $O(1)$. We discuss implications for volcanic plumes and pyroclastic currents. Our study suggests that clustering and related enhanced or hindered particle settling velocities should be considered in models of volcanic phenomena and that drag law corrections are needed for reliable predictions and hazard assessment.

Plain Language Summary

The propagation of turbulent dust storms, snow surge avalanches, dilute pyroclastic density currents, and volcanic plumes is controlled by the particle concentration, which depends on the particle settling velocity. Most numerical models consider only theoretical single-particle settling velocities. However, in the presence of neighboring particles, the settling velocity is strongly affected by gas-particle and particle-particle interactions. Our main objective is to unravel the relationship between the particle concentration and the particle settling velocity. We present laboratory experiments, in which the local particle concentration is measured using two independent techniques. We observe two settling mechanisms depending on the coupling of the particles with the gas, namely, hindered settling or cluster-induced enhanced settling. These mechanisms result in settling velocities significantly different from those of single particles. As an illustrative example, we consider the fall deposit of the 10.5 ka Plinian eruption at Llaima (Chile) and argue that clusters of centimeter-sized clasts had enhanced settling velocities similar to those of 10-20 cm diameter clasts. Our main conclusion is that mechanisms causing enhanced or hindered particle settling velocities should be considered for accurate models of geophysical processes, possibly through drag law corrections.

1 Introduction

Dust storms, snow surge avalanches, dilute pyroclastic density currents, and volcanic plumes are examples of geophysical flows of particles in a turbulent gas. The settling velocity of particles is essential because it controls the particle concentration and hence the dynamics of these flows. If the particles are suspended by the fluid, the dynamics of the mixture is controlled by the coupling of the fluid and the particles as well as interparticle collisions. Instead, if the particles are not suspended, they settle to form a deposit or a dense basal flow controlled by particle-particle interactions. Experimental and numerical studies revealed that the particle settling velocity may increase (Wang & Maxey, 1993; Dey et al., 2019) or decrease (Nielsen, 1993; Fornari et al., 2016; Dey et al., 2019) depending on the degree of turbulence, and it can be lower (Marchetti et al., 2022) or higher (Del Bello et al., 2017) than predicted theoretically for a single par-

67 ticle depending on the particle size, shape, and concentration. Actual particle settling
68 velocities different from theoretical velocities used in models may be a cause of discrep-
69 ancies between observed and simulated volcanic fall deposits (Tadini et al., 2020, 2022)
70 and this issue is critical in the context of hazard assessment.

71 Dilute turbulent gas-particle mixtures are known to exhibit regions of higher parti-
72 cle concentrations called clusters, which affect the mixture dynamics and the particle
73 settling velocity (Fullmer & Hrenya, 2017; Brandt & Coletti, 2022). The key mechanisms
74 that lead to particle clustering can be divided into two categories: dissipation of gran-
75 ular temperature (i.e., fluctuations in particle velocities) due to inter-particle collisions,
76 and relative motion between the particles and the continuous fluid. Only a few numer-
77 ical and experimental studies have addressed the effects of clustering on the particle set-
78 tling velocity and they revealed that clusters had a fall velocity greater than that of a
79 single particle (Wang & Maxey, 1993; Uhlmann & Doychev, 2014; Breard et al., 2016;
80 Fornari et al., 2019; Fong & Coletti, 2022). In this context, recent experiments showed
81 that the lifespan of clusters in mixtures of particles suspended by an ascending air flow
82 played a fundamental role in setting a critical concentration of particles above which ad-
83 ditional particles were not maintained in the mixtures (Weit et al., 2019; van den Wilden-
84 berg et al., 2020; Fong & Coletti, 2022).

85 How clustering controls the particle settling velocity and the dynamics of dilute tur-
86 bulent geophysical flows remains an open question. The major challenge to addressing
87 this issue experimentally is to obtain reliable values for the solid volume fraction inside
88 3D suspensions and over a range of controlling parameters. This is due the relatively large
89 size of the particles ($\sim 100 \mu\text{m}$) and their concentration ($\sim 0.1\text{-}10 \text{ vol.}\%$), which results
90 in scattering of light and makes optical observation complicated (Fong & Coletti, 2022).
91 Therefore, experimental studies are often restricted to very dilute suspensions with parti-
92 cle concentrations $\ll 1 \text{ vol.}\%$ (Fong & Coletti, 2022; Del Bello et al., 2017) in which
93 particle-fluid (two-way) interactions are expected to dominate. In the present study, we
94 use two independent techniques to investigate particle settling in suspensions with parti-
95 cle concentrations $\sim 0.1\text{-}3 \text{ vol.}\%$: acoustic probing (van den Wildenberg et al., 2020)
96 and local pressure measurements. We quantify the relationship between the settling ve-
97 locity (i.e., the flow velocity necessary to suspend the particles) and the concentration
98 of particles. We find that the settling velocity in suspensions of $78 \mu\text{m}$ particles with Stokes
99 number $O(1)$ increases with the local particle concentration and is higher than that of
100 a single particle, hence revealing enhanced settling. In contrast, suspensions of $467 \mu\text{m}$
101 particles with Stokes number $O(100)$ experience hindered settling. We discuss implica-
102 tions of our results for geophysical flows, focusing on volcanic mixtures generated by ex-
103 plosive eruptions.

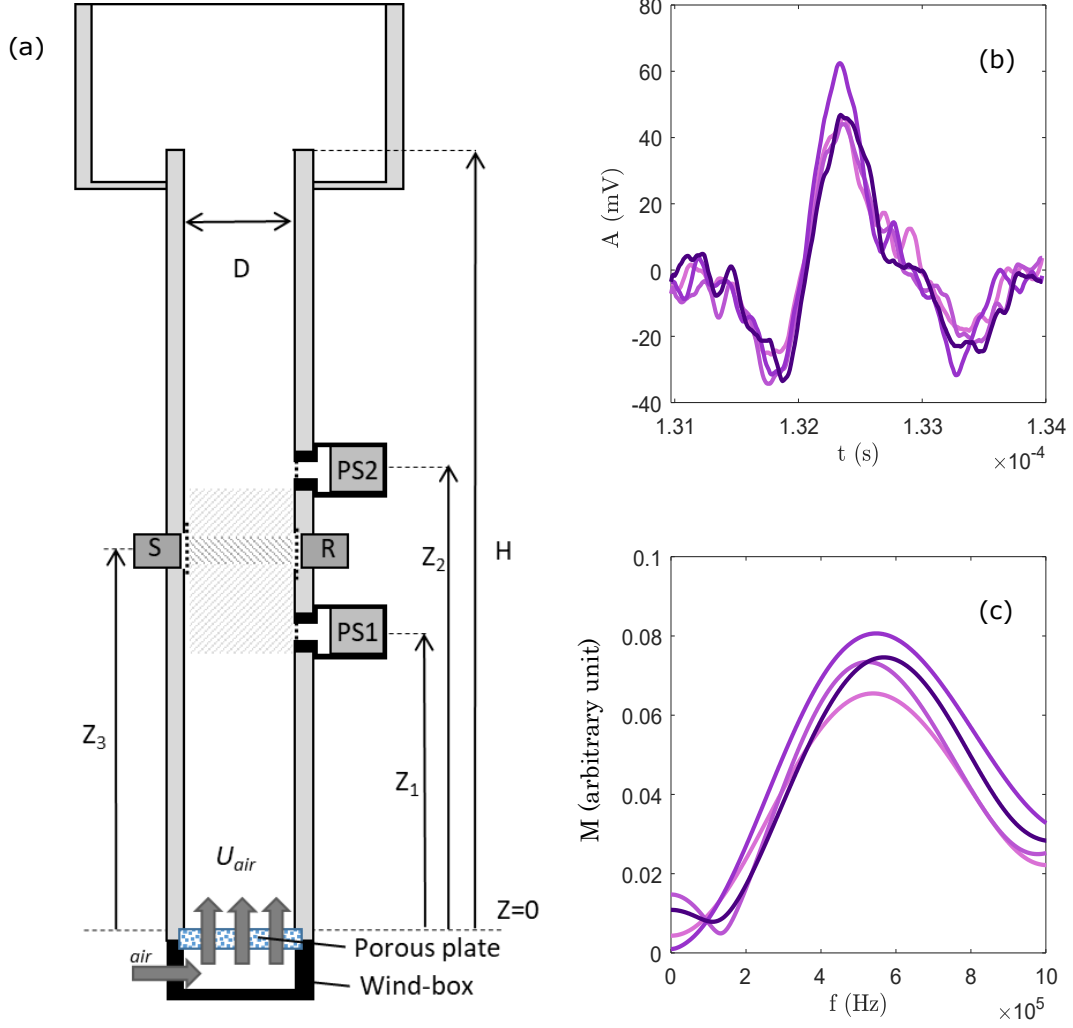


Figure 1. (a) The experimental setup is a cylindrical pipe of height $H=1$ m and inner diameter $D=4$ cm. An air flow is delivered into the container via a wind-box and a porous plate, and a large cylinder at the top of the pipe allows the air velocity to decrease. Interstitial air pressure is measured by two piezo-resistive sensors (PS) placed at heights $Z_1=51.5$ cm and $Z_2=56.5$ cm. Two piezo-electric transducers (S and R) placed at position $Z_3=54$ cm (in between PS_1 and PS_2) are used to measure acoustic wave propagation through the suspension. The volume probed by the local fluid pressure measurements is depicted in dashed light grey, and the volume probed by the acoustic monitoring is depicted in dashed dark grey. (b) Amplitude versus time for four typical (coherent) sound waves measured in different suspensions of glass particles with $d=467$ μm and $\phi_L \sim 1\%$. Here $t=0$ corresponds to the time at which the ultrasonic pulse is sent by the source transducer. (c) Magnitude versus frequency obtained from fast Fourier transforms of the four the sound waves in (b).

104

2 Methods

105

2.1 Experimental device and material

106

107

All experiments were performed at room temperature in a cylindrical pipe with a height (H) of 1 m and an inner diameter (D) of 4 cm (Fig. 1). At the base of the pipe

108 is a porous plate and the ensemble is placed on a wind-box. It was shown that the ge-
 109 ometry of the air inlet is important for the stability of the air flow (Bagheri et al., 2013;
 110 Bonadonna & Phillips, 2003) and, therefore, the wind-box has the same inner diameter
 111 as the pipe. An air supply system delivered mean air flow velocities (U) through the wind-
 112 box and the porous plate into the pipe. For particle sizes smaller than 300 μm , we used
 113 the compressed air available in the laboratory and set the air flow using debit controllers
 114 that had a precision of less than 1 L/min. For particle sizes larger than 300 μm , a com-
 115 pressor (Worthington Creyssensac RLR 35B) was used in combination with a dedicated
 116 debit controller. This controller had a minimum increment of 10 L/min (with a preci-
 117 sion of about 2 L/min). The porous plate had a thickness of 10 mm and a pore size of
 118 20 μm . The influence of the porous plate on the turbulent structures of the airflow is not
 119 trivial. We expect that when the air exits the plate the eddy size will be roughly equal
 120 to the size of the pores, and the eddy size grows -as the air flows upwards in the pipe-
 121 to about half the pipe's diameter.

122 At the top of the pipe, a large diameter cylinder ($\sim 2D$) allowed the air velocity
 123 to decrease and prevented the loss of particles from the pipe. The pressure of the inter-
 124 stitial air was measured by two piezo resistive sensors installed at heights $Z_1= 51.5$ cm
 125 and $Z_2= 56.5$ cm above the porous plate. The sensors were placed in adapters, which
 126 were in direct contact with the suspension via a small hole covered by a grid (36 μm mesh
 127 size) to prevent particles entering the adapter and colliding with the sensor. Furthermore,
 128 two piezo-electric transducers placed at position $Z_3= 54$ cm (in between pressure sen-
 129 sors PS_1 and PS_2) were used to measure acoustic wave propagation through the sus-
 130 pension. One transducer was used as an acoustic source (S) while the second transducer
 131 (R) detected the wave at a distance $L \sim 0.04$ m from the source. To avoid pollution of
 132 the acoustic signal by particles colliding against the transducer-face, 36 μm mesh size
 133 grids were installed on the inside wall of the container in front of the transducers. A typ-
 134 ical experiment is performed as follows. First, a known mass of glass beads is poured into
 135 the pipe, and a mean input solid volume fraction ϕ_i is calculated from the mass and the
 136 assumption that the beads are homogeneously distributed over the volume of the cylin-
 137 der. Then, the particles are suspended in air by a vertical upward air flux at velocity U
 138 and the fluid pressure is measured using the two pressure sensors. Additionally, 400 short
 139 pulses are sent by a piezo-electric transducer and the propagating pulses are measured.
 140 For each particle size, the experiment is repeated 3 times. We experimented with nearly
 141 mono disperse spherical glass particles with density $\rho_2 \sim 2500$ kg/m³ and mean diam-
 142 eters d of 49, 78, 206, 308 and 467 μm (sieved between: 45-53, 75-80, 200-212, 300-315,
 143 450-475 μm , respectively). We filmed the suspensions with a high-speed Photron Fast-
 144 cam SA3 video camera, with resolution of 0.77 mm per pixel, located at 30 cm from the
 145 pipe. Movies were acquired at a rate of 250 frames per second and a spatial resolution
 146 of 58 x 882 pixels. Improved contrast was achieved by placing the pipe about 50 cm in
 147 front of a 40 W white light panel of size 59.5 x 59.5 cm, of which 54.4 x 54.4 cm was the
 148 lighting surface.

149 2.2 Interstitial fluid pressure data

150 Interstitial fluid pressure arises from air-particle differential motion and the related
 151 drag. In each experiment, the generated fluid pressure is measured over time using the
 152 pressure sensors that take 500 samples each with a sampling rate of ~ 50 Hz. The bulk
 153 solid volume fraction above each sensor may be obtained from the time-averaged pres-
 154 sure (P) via: $\phi_b = P/(\rho_2 g(H - Z_i))$ (Weit et al., 2019). However, this implies that the
 155 suspension is homogeneous, which is not necessarily true. Therefore, in this study we cal-
 156 culate a local solid volume fraction from the pressure measurements of two pressure sen-
 157 sors (PS_1 and PS_2), as follows: $\phi_L = \Delta P/(\rho_2 g \Delta Z)$ with $\Delta P = P_1 - P_2$ and $\Delta Z =$
 158 $Z_2 - Z_1 = 5$ cm (the indices indicate the pressure sensors) and the volume probed is
 159 depicted in Fig. 1. From $\phi_L(t)$ it can be observed that a quasi steady state is attained
 160 (see Supplementary Information section 1), and only for the smaller particles do we ob-

Table 1: Symbols and their units

Symbol	Units	Definition
C_d	-	Drag coefficient for a single particle
d	μm	Particle diameter
D	m	Inner diameter of pipe
H	m	Height of pipe
U	m.s^{-1}	Mean air flow velocity
U^*	m.s^{-1}	Mean particle settling velocity in the suspension
U_m	m.s^{-1}	Air velocity corresponding to ϕ_{Lm}
U_t	m.s^{-1}	Terminal settling velocity of a single particle
$U_{cluster^*}$	m.s^{-1}	Reduced cluster velocity (velocity in laboratory reference frame)
$U_{cluster}$	m.s^{-1}	Cluster velocity ($U_m + U_{cluster^*}$)
Re_p	-	Particle Reynolds number
St	-	Stokes number
T	s	Cluster lifetime
Z	m	Elevation in pipe
α	m^{-1}	Attenuation coefficient
β	-	Effective drag coefficient
η	Pa.s	Gas dynamic viscosity
κ_1	N.m^{-2}	Air compressibility
κ_2	N.m^{-2}	Solid compressibility
ρ_1	kg.m^{-3}	Air density
ρ_2	kg.m^{-3}	Solid density
ϕ	-	Particle volume fraction
ϕ_c	-	Maximum particle volume fraction that can be suspended
ϕ_i	-	Particle volume fraction assuming particles are homogeneously distributed in pipe
ϕ_L	-	Local particle volume fraction
ϕ_{Lm}	-	Maximum local particle volume fraction
k	m^{-1}	complex wavenumber
σ	-	density ratio

161 serve a small drift due to loss of particles during the experiment. A time averaged ϕ_L
 162 may thus be calculated by averaging the 500 samples (~ 10 s).

163 2.3 Acoustic measurements

164 In each experiment, we measure the propagation of 400 short acoustic pulses with
 165 central frequency $f = 0.5$ MHz and repetition time of 30 ms. For each transmitted sig-
 166 nal, the frequency dependent attenuation coefficient $\alpha(f)$ is determined from the fast Fourier
 167 transform (FFT) using: $\alpha(f) = (-1/D) \ln(A_{sus}/A_f)$, with A_f and A_{sus} the amplitudes
 168 obtained from the FFT for acoustic signals propagating through a pure fluid phase (air)
 169 and the granular suspension, respectively. The attenuation coefficient spectra are aver-
 170 aged over all 400 pulses to obtain a mean attenuation spectrum for each experiment.

171 We interpret our experimental measurements with two models. For more details
 172 we refer readers to van den Wildenberg et al. (2020) and references therein.

173 (i) The coupled-phase hydrodynamic model developed by Urick (1948) considers
 174 a system with a volume fraction ϕ of solid particles with density ρ_2 and compressibil-
 175 ity κ_2 , suspended in a viscous continuous phase with density ρ_1 and compressibility κ_1 .
 176 In the long wavelength limit ($\lambda/d \gg 1$), the ultrasound attenuation coefficient in such
 177 a system is approximated as (Urick, 1948):

$$\alpha = \phi \left[\frac{1}{6} k^4 a^3 + k(\sigma - 1)^2 \frac{s}{s^2 + (\sigma + \tau)^2} \right] + \zeta \quad (1)$$

178 where $a = d/2$, the wavenumber $k = \omega/v$ with ω the angular frequency, $v \sim 349$ m/s
 179 the sound velocity in air, $\sigma = \rho_2/\rho_1$, $\tau = (1/2) + (9/4)(\delta/a)$, and $s = (9/4)[(\delta/a) +$
 180 $(\delta/a)^2]$. Here $\delta = \sqrt{2\eta/(\omega\rho_1)}$ is a characteristic viscous (shear wave) length, with η the
 181 dynamic viscosity of the continuous phase, and ζ is a frequency independent offset (van den
 182 Wildenberg et al., 2020).

183 (ii) The ECAH theory is based on scattering models at the microscopic scale ($\lambda/d \sim$
 184 1) developed by Epstein and Carhart (1953) and Allegra and Hawley (1972). The model
 185 describes the interactions of scattered, visco-inertial, and thermal fields with a single par-
 186 ticle and its surrounding medium (Epstein & Carhart, 1953; Allegra & Hawley, 1972; Ying
 187 & Truell, 1956; Challis et al., 2005). As the density contrast between the two phases (air
 188 and glass) is very high, we neglect the thermal contribution (Challis et al., 2005). Fi-
 189 nally we combine the ECAH theory with a multiple scattering theory to correlate the
 190 complex wavenumber (k) to the frequency dependent α via:

$$\alpha = \zeta + Im \left[\sqrt{k^2 + \frac{3\phi}{a^3} f(0) + \frac{9\phi^2}{4a^6 k^2} (F^2(0) - F^2(\pi))} \right] \quad (2)$$

191 Here Im signifies the imaginary part and $F(0)$ and $F(\pi)$ are the forward and backward
 192 scattering amplitudes of the individual particles, respectively. The scattering amplitudes
 193 are calculated from the scattering coefficients of the various types of waves scattered from
 194 an individual particle, and we consider scattering and viscous/inertial losses and neglect
 195 thermal conduction losses. ϕ is then calculated from the experimental acoustic data by
 196 fitting the theoretical α from the models using Matlab's least-squares curve fitting tools.
 197 In the dilute suspensions considered here, the additional free fitting parameter $\zeta \sim 0$ -
 198 1.

199 3 Results

200 3.1 Acoustic probing and local fluid pressure measurements

201 We start by comparing the local solid volume fraction ϕ_L obtained by local fluid
 202 pressure measurements and acoustic attenuation measurements. To do so, we introduce
 203 a known mass of particles ($d= 49, 78, 206, 307$ or $467 \mu\text{m}$) into the container and choose
 204 U so that ϕ_L obtained from the fluid pressure is about 1%. Then, we measure the propa-
 205 gation of 400 acoustic pulses. The similarity between the acoustic pulse signals demon-
 206 strates the reproducibility of the sound propagation through the suspension (Fig. 1b)
 207 and spectral analysis of the sound signals evidences a single peak around $f_c \sim 0.5$ MHz
 208 (Fig. 1c). The attenuation coefficient α , calculated from the spectral analysis, increases
 209 with the frequency (Fig. 2a). In order to infer ϕ_L we compare $\alpha(f)$ with existing the-
 210 oretical models. For the particles smaller than $200 \mu\text{m}$, both the Urlick and ECAH mod-
 211 els predict well the experimental data (Fig. 2a). In contrast, for the larger particles, only
 212 the ECAH model appears to be able to describe our data (Fig. 2a). For each particle
 213 size, a mean ϕ_L is calculated from the pressure measurements and from the acoustic mon-
 214 itoring by averaging 3 experiments. Importantly, we find overall a good agreement be-
 215 tween ϕ_L obtained by the local fluid pressure and acoustic methods (Fig. 2b).

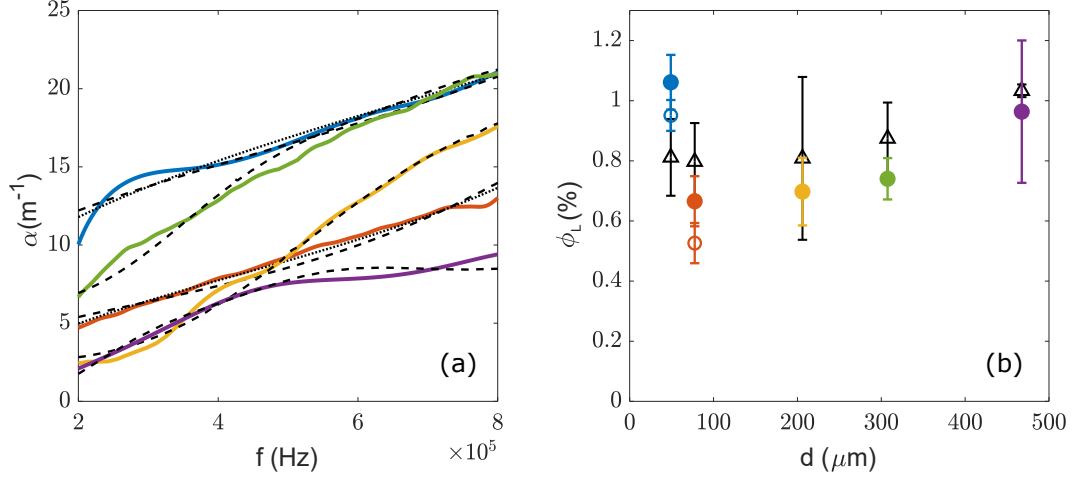


Figure 2. Acoustic wave attenuation in suspensions of glass beads. (a) Example traces of α versus frequency for suspension of glass particles in air (blue: $d= 49 \mu\text{m}$, orange: $d= 78 \mu\text{m}$, yellow: $d= 206 \mu\text{m}$, green: $d= 308 \mu\text{m}$, purple: $d= 467 \mu\text{m}$). The dotted lines represent the fits of $\alpha(f)$ by the Urick model (Eq.1). The dashed lines represent the fits of $\alpha(f)$ by the ECAH44 model (Eq.2). (b) ϕ_L averaged over 3 experiments as a function of the particle diameter. Solid dots represent ϕ_L obtained from the ECAH44 model, open dots represent ϕ_L obtained from the Urick model, and triangles represent the ϕ_L obtained from the local fluid pressure. The error bars show the standard deviations over the experiments. Colors correspond to those in (a).

216 To test the applicability of these techniques over a wider range of particle concentrations,
 217 a mass of particles of 160.08 g (corresponding to $\phi_i = 5\%$) is introduced into the
 218 container at $U=0$. Subsequently U is slowly ramped-up and the acoustic wave prop-
 219 agation and the fluid pressure are measured. We use glass beads of size $d= 78 \mu\text{m}$ and
 220 $467 \mu\text{m}$, and the experiment is repeated 3 times. Traces of $\alpha(f)$ reveal that the sound
 221 attenuation increases with U as more particles enter the volume probed by the acous-
 222 tic wave (Fig. 3a). Since the ECAH model appears to work for both particle sizes, we
 223 will use this model to infer ϕ_L from $\alpha(f)$. As before, we determine a mean ϕ_L for the pres-
 224 sure measurements and for the acoustic monitoring by averaging over all experiments.
 225 Figure 3b shows ϕ_L as a function of U . Overall, we find that ϕ_L obtained by the two tech-
 226 niques are similar for all the concentrations tested. For the particles $d= 78 \mu\text{m}$, ϕ_L is
 227 first nearly 0 for the lowest flow velocities, and above $U \sim 0.4 \text{ m/s}$ it increases until a
 228 maximum of $\phi_L \sim 0.5\%$ is reached at $U \sim 0.58 \text{ m/s}$, above which ϕ_L decreases as the
 229 particles are dragged above the position of the sensors. For the suspensions of larger par-
 230 ticles $d= 467 \mu\text{m}$, we observe a similar behavior, but for higher U . One important ob-
 231 servation is that, even though the ϕ_i is the same (5%), the maximum ϕ_L obtained dif-
 232 fers significantly for the two particle sizes. For the $d= 467 \mu\text{m}$ particles we find that $\phi_L \sim$
 233 4% ($\sim \phi_i$), while for the $d= 78 \mu\text{m}$ particles $\phi_L \sim 0.45\%$ almost ten times smaller than
 234 ϕ_i .

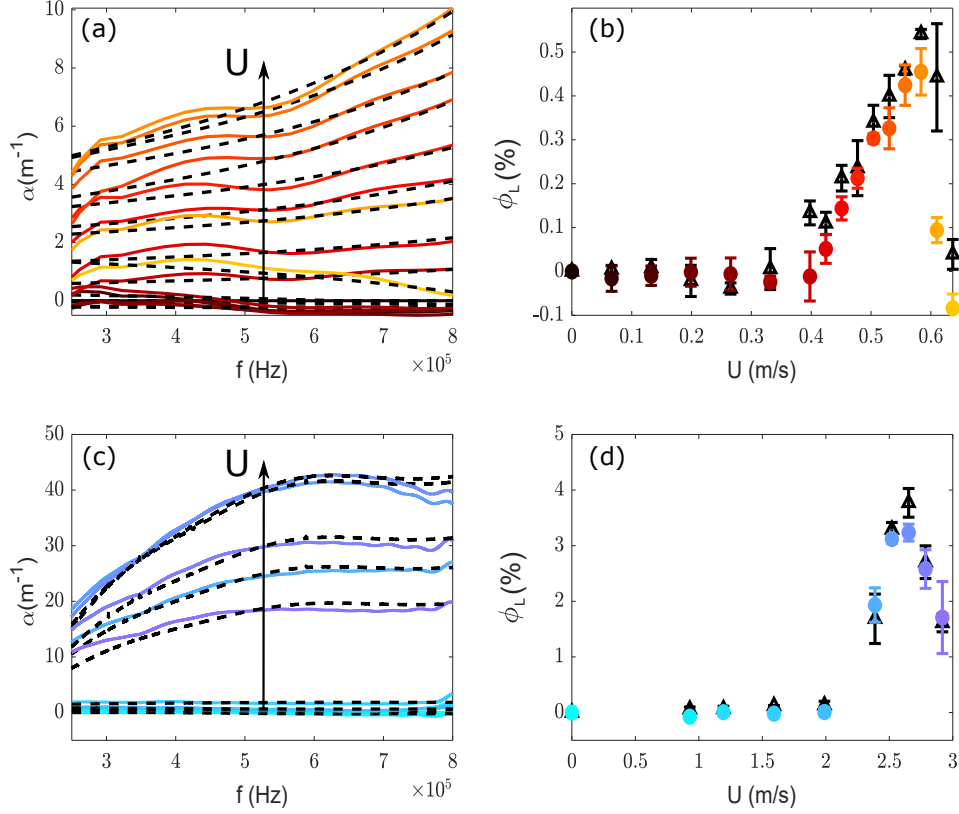


Figure 3. (a) Attenuation coefficients versus frequency in a suspension of $d = 78 \mu\text{m}$ glass beads for increasing U . (b) ϕ_L obtained from fits of $\alpha(f)$ in (a) by the ECAH44 model (black dashed lines in a). The black triangles are ϕ_L obtained from local fluid pressure. (c) Same as (a) for $d = 467 \mu\text{m}$ glass beads. (d) ϕ_L obtained from fits in (c) by the ECAH44 model (black dashed lines in c). The black triangles are ϕ_L obtained from the local fluid pressure. Error bars represent the standard deviations over three experiments.

235

3.2 Local solid volume fraction and clustering

236

237

238

239

240

241

242

243

244

245

246

Next, we investigate the relationship between the maximum local solid volume fraction ϕ_{Lm} , the air velocity, and the particle size. Experiments are repeated for varying ϕ_i and for simplicity we use only fluid pressure measurements to calculate ϕ_L . The resolution in the experiments is limited by the minimal increments of the flow meter, from which the error bars in U are determined. In suspensions of $78 \mu\text{m}$ particles, we find that, for a given ϕ_i , ϕ_L increases with U to ϕ_{Lm} at U_m , after which it decreases rapidly (Fig. 4a). Importantly, for increasing ϕ_i , both the ϕ_{Lm} and U_m increase (Fig. 4c,d). For the suspensions of $467 \mu\text{m}$ particles, a similar behavior is found for ϕ_L and ϕ_{Lm} , with ϕ_L increasing with U until its maximum value ϕ_{Lm} at U_m , and increasing ϕ_i leads to a higher ϕ_{Lm} (Fig. 4b,e). However, in contrast to the smaller particles, U_m appears to decrease with increasing ϕ_i (Fig. 4f).

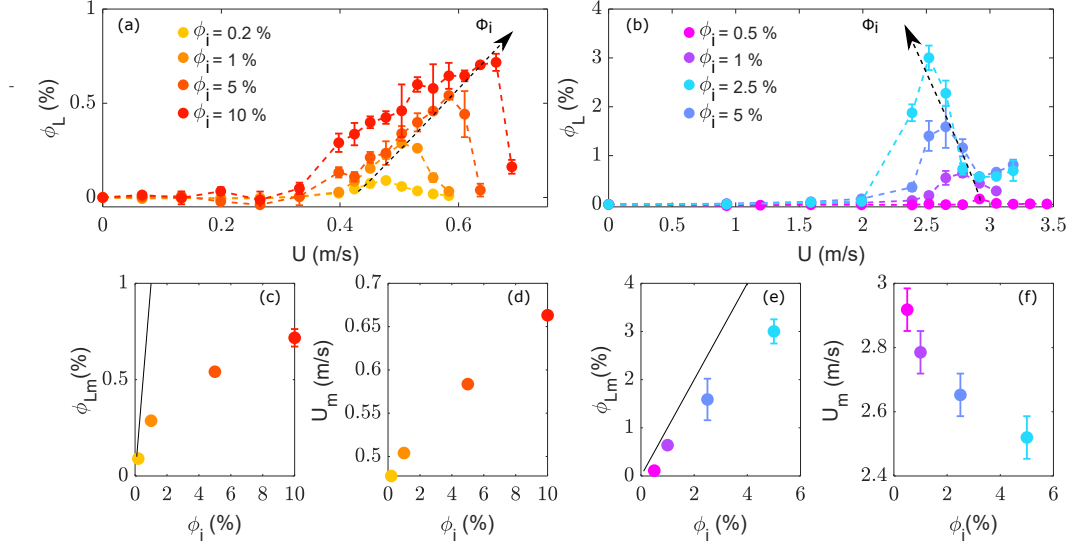


Figure 4. ϕ_L calculated from local pressure measurements and presented as a function of the air velocity U . (a) Suspensions of $d=78 \mu\text{m}$ glass for increasing ϕ_i [$\phi_i=0.2\%$ (yellow), 1% (light orange), 5% (dark orange), 10% (red)]. The dashed arrow illustrates the shift of the curves to the right for increasing ϕ_i . (b) Suspensions of $d=467 \mu\text{m}$ glass beads [$\phi_i=0.5\%$ (magenta), 1% (dark purple), 2.5% (light purple), 5% (blue)]. The dashed arrow illustrates the shift of the curves to the left for increasing ϕ_i . (c) The maximum local concentration ϕ_{Lm} versus ϕ_i from the data in (a). The line represents $\phi_{Lm} = \phi_i$. (d) The air velocity U_m corresponding to ϕ_{Lm} versus ϕ_i from the data in (a). (e) The maximum local concentration ϕ_{Lm} versus ϕ_i from the data in (b), the line represents $\phi_{Lm} = \phi_i$. (f) The air velocity U_m corresponding to ϕ_{Lm} versus ϕ_i from the data in (b). Error bars of ϕ are the standard deviations over the experiments, error bars in U_m are the increment in the air velocity (for the $d=78 \mu\text{m}$ particles the error bars of U_m are the size of the symbols).

247 We filmed each suspension at ϕ_{Lm} and the corresponding U_m , focusing on the
 248 region between PS_1 and PS_2 . Frames from those movies are presented in Fig. 5 and show
 249 that regions with high particle concentrations (clusters) are present in all the suspen-
 250 sions, except in those with the lowest ϕ_{Lm} . This supports the idea that cluster lifespan
 251 plays an important role in the maximal concentration of particles that can be suspended
 252 (ϕ_c) as well as in the formation of dense beds at the bottom of the suspension (van den
 253 Wildenberg et al., 2020; Fong & Coletti, 2022).

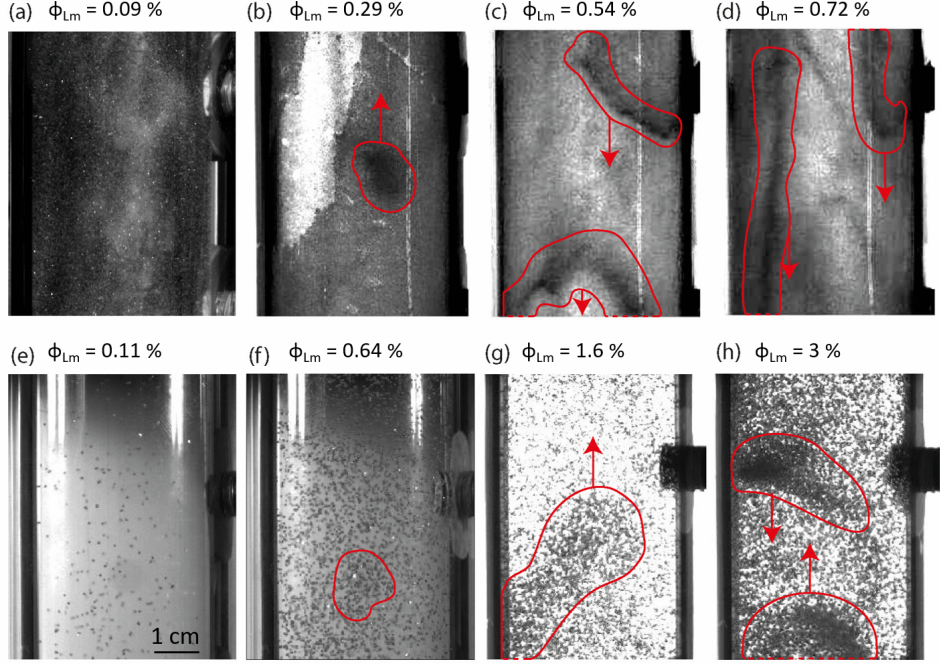


Figure 5. Frames from movies of suspensions with varying ϕ_i at the relevant U_m . The movies are focused on the region between pressure sensors PS₁ and PS₂. (a)-(d) suspensions of 78 μm particles with $\phi_{Lm} = 0.09, 0.29, 0.54, 0.72\%$, respectively. (e)-(h) suspensions of 467 μm particles with $\phi_{Lm} = 0.11, 0.64, 1.6, 3\%$, respectively. Particles are black against a white background, except for in (a) where the particles are white against a black background. Denser regions of particles are outlined in red and the arrows indicate the direction of cluster movement.

254 A detailed investigation of the size, shape, and particle concentration of clusters
 255 is beyond the scope of this paper due to the spatial resolution of the images and is further
 256 complicated by the limited penetration of the light through the suspension. We thus
 257 provide a phenomenological description of the suspensions. Clusters in the suspensions
 258 of small particles tend to be elongated and relatively concentrated by comparison to clusters
 259 observed in the suspension of larger particles which are more rounded and less concentrated
 260 (Fig.5). In circulating fluidized bed risers (with higher particle concentrations
 261 compared to our experiments), cluster size shows no systematic variations with the particle
 262 size nor the riser size (Cahyadi et al., 2017; Berruti et al., 1995). Instead, it has been
 263 shown to, in some cases, vary with the radial position due to variations in radial velocity
 264 as particles go up in the middle and down on the sides (Cahyadi et al., 2017; Berruti
 265 et al., 1995). Our experiments show similar cluster trajectories (Supplementary Information
 266 section 4 and supplementary movies), however, variations in cluster size remain
 267 elusive. These are qualitative impressions and care should be taken when interpreting
 268 2D projections of 3D structures.

269 In order to accurately determine the cluster fall velocity ($U_{cluster}$), it is necessary
 270 to consider long trajectories. Therefore, we filmed the suspensions of $d = 78 \mu\text{m}$ particles
 271 at $\phi_L = 0.7\%$ and $U_m = 0.66 \text{ m/s}$, and $d = 467 \mu\text{m}$ particles at $\phi_L = 3\%$ and
 272 $U_m = 2.5 \text{ m/s}$, imaging the whole pipe at a frame rate of 250 Hz (see Supplementary
 273 movies). The duration of those movies corresponds to the time over which a pressure
 274 measurement was performed. Small particles are lost during the time of the movie, which
 275 results in progressively lighter images. However, this loss is small and does not change
 276 significantly ϕ_L . To study the motion of the clusters we first produce a kymograph, which

277 is an intuitive way to represent the dynamics of the clusters during the movie in a sin-
 278 gle image. For each image of the movie, we plot the light intensity along a line in the
 279 Z-direction near the center of the pipe (Fig. 6). Clusters that ascend and descend are
 280 depicted in the kymograph as trajectories with a positive slope and a negative slope, re-
 281 spectively. The trajectories of these clusters show that their motion is mostly smooth
 282 and continuous. We thus determine the slope and length of the trajectories correspond-
 283 ing to the settling velocity $U_{cluster^*}$ and lifetime T of the clusters. Note that $U_{cluster^*}$
 284 is a reduced settling velocity owing to the ascending air flow. We use ImageJ and the
 285 available plugin *RidgeDetection* (Steger, 1998), which is an algorithm developed for de-
 286 tecting ridges and lines. We consider trajectories with a minimal length of 70 frames (cor-
 287 responding to 0.28 s), so that their slope is well defined. We find that the identified tra-
 288 jectories converge for 78 μm particles with parameters linewidth=3, lower threshold =
 289 0.2 and upper threshold = 1.4. For 467 μm particles, a linewidth=3, lower threshold =
 290 0.2 and upper threshold=7.1 are used. For each movie, we track about 140 descending
 291 clusters and show the results in histograms in Fig. 6b,c. Descending clusters appear sig-
 292 nificantly more numerous (more than 70% of the clusters descend, see Fig.6e) and in gen-
 293 eral we have the impression that they are more concentrated than ascending clusters (Sup-
 294 plementary movies). The average lifetime of clusters is about 0.6 s and is the same in sus-
 295 pensions of 78 μm particles and in suspensions of 467 μm particles. However, the mean
 296 settling velocity of descending clusters, as determined from averaging all positive $U_{cluster^*}$
 297 for a given particle size, in suspension of 78 μm particles is $\bar{U}_{cluster^*} \sim 0.9$ m/s, while
 298 in suspensions of 467 μm particles we find that $\bar{U}_{cluster^*} \sim 1.1$ m/s.

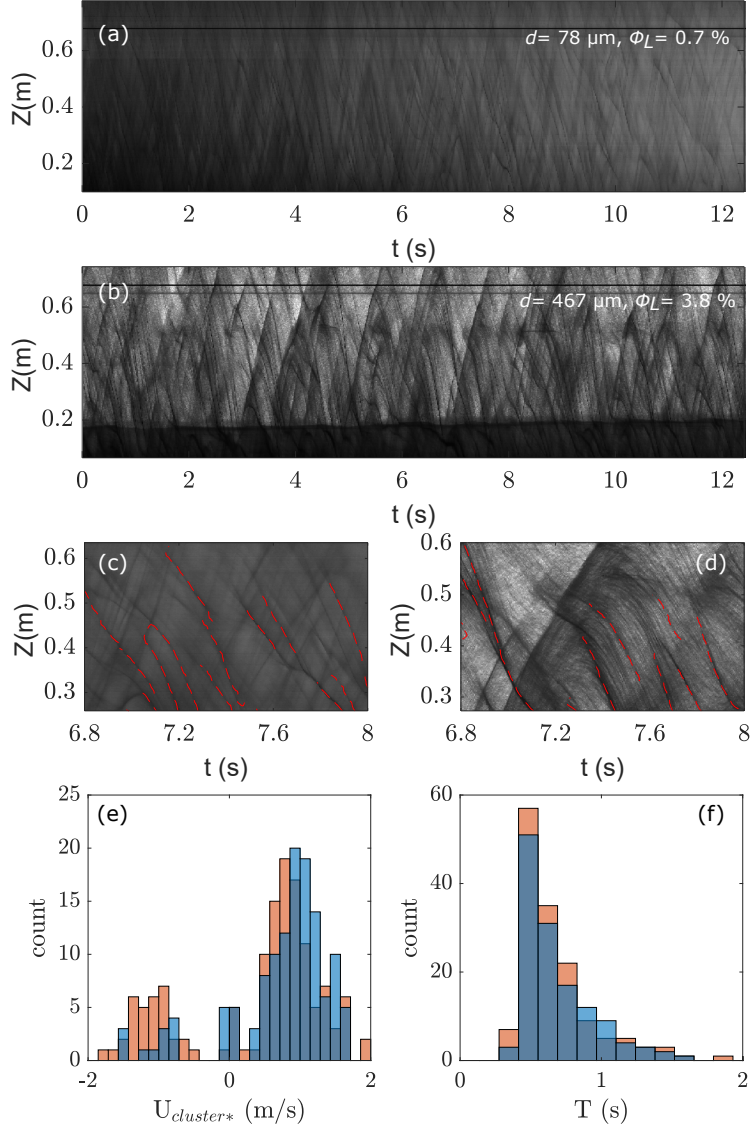


Figure 6. Kymographs of clusters in suspensions of (a) $d = 78 \mu\text{m}$ particles, and, (b) $d = 467 \mu\text{m}$ particles. (c and d) Zoom of the kymograph in (a) and (b), trajectories of clusters are shown by the red dashed lines. (e) Histogram of the reduced velocities of tracked clusters. Negative velocities correspond to ascending clusters, while positive velocities correspond to descending clusters. Most of the tracked clusters descend. (f) Histogram of lifetime (T) of descending clusters. Red and blue (transparent) colors correspond to suspensions of $78 \mu\text{m}$ and $467 \mu\text{m}$ particles, respectively.

299

4 Discussion

300

4.1 Acoustic probing and local fluid pressure measurements

301

302

303

304

305

The solid volume fraction in particle suspensions is difficult to measure experimentally. Our first main result is the comparison of two independent approaches to determine the local solid volume fraction (ϕ_l) in dilute but optically opaque suspensions of particles in air, namely (i) local fluid pressure measurements and (ii) acoustic probing. These techniques yield similar local solid volume fractions for a wide range of particle

306 sizes and particle concentrations. They thus present tools for investigating the solid vol-
 307 ume fraction in laboratory experiments. Local fluid pressure measurements have the ad-
 308 vantage that they offer ready access to the local solid volume fraction, without the need
 309 of many additional parameters such as, for example, the particle size or the viscosity of
 310 the fluid. Its main limitation is that it can be used only when there is a significant in-
 311 terstitial fluid pressure. Instead, acoustic monitoring can be used in the absence of fluid
 312 pressure. It is, however, more laborious to apply and needs more physical parameters,
 313 which may not be known. Moreover, in suspensions of particles larger than $200\ \mu\text{m}$ the
 314 Urick model yields poor fits with unreasonably low ϕ_L indicating that this model fails.
 315 Under the assumption that the viscosity/inertia is responsible for the acoustic energy
 316 loss, only the second term in Eq. 1 (viscous-inertial loss) may be used (Pierce et al., 2016).
 317 Indeed, the use of only this term captures our data $\alpha(f)$ for the larger particles. How-
 318 ever, the inferred $\phi_L \sim 3\text{-}4\%$ is larger than the $\sim 1\%$ obtained from the ECAH model
 319 and from local pressure measurements (Supplementary Information section 2). Further
 320 work is needed to address this issue.

321 **4.2 Local solid volume fractions and particle settling velocities**

322 The second main result is the dependence of U_m on the maximum local particle
 323 concentration ϕ_{Lm} , as observed in Fig. 4a&b, and for clarity we present cross plots in
 324 Fig. 7a&c. For the $78\ \mu\text{m}$ particles, U_m increases rapidly with increasing ϕ_{Lm} (Fig.7a),
 325 indicating that these particles settle faster at higher particle concentrations. Instead, for
 326 the $467\ \mu\text{m}$ particles, U_m decreases with increasing ϕ_{Lm} (Fig.7c), indicating that these
 327 larger particles settle slower at higher concentrations. In the following sub-sections we
 328 will discuss these findings in detail.

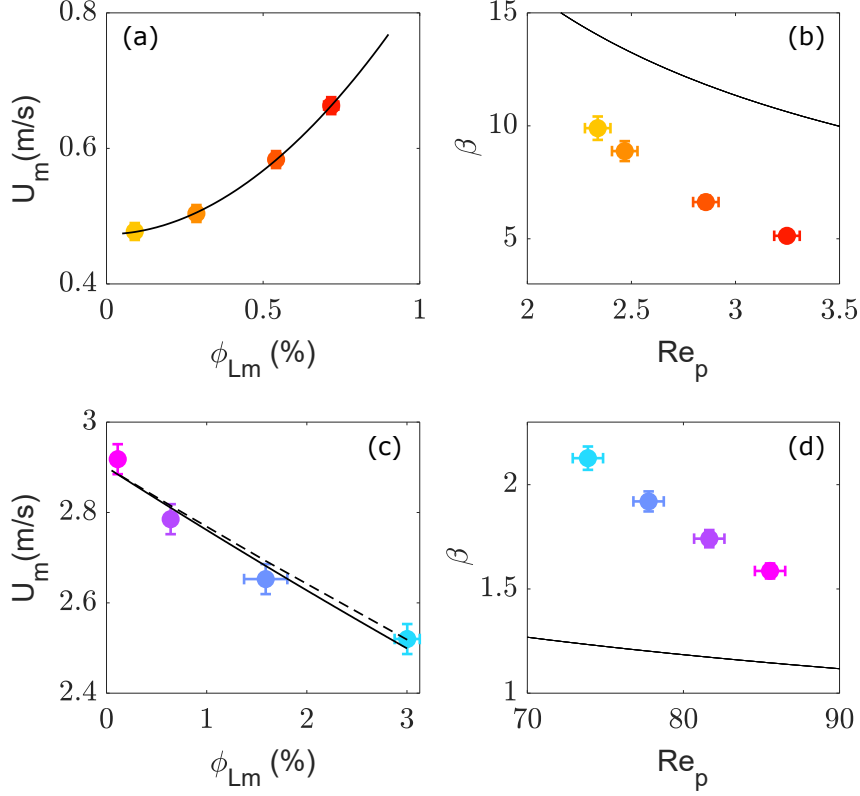


Figure 7. (a) Cross-plots of U_m versus ϕ_{lm} for suspensions of 78 μm particles (data from Fig. 4a). The solid black curve is a power law fit. (b) Effective drag coefficient β calculated from (a) versus the Re_p . The black curve is the estimated drag on a single particle via Abraham's contribution. (c) Cross-plot of U_m versus ϕ_{lm} (data from Fig. 4b) for suspensions of 467 μm particles. Solid black curves are fits of $U_m = p_1(1 - \phi_{Lm})^{p_2}$ and theoretical predictions using $U^* = p_1(1 - \phi)^n$ with $n = (5.1 + 0.27Re_p^{0.9})/(1 + 0.1Re_p^{0.9})$ (dashed curve). (d) β calculated from (c) versus the Re_p . The black curve is the estimated drag on a single particle via Abraham's contribution (see main text).

329

4.2.1 Air flow regime

330

The hydrodynamics of the macroscopic air flow in our device is described by the Reynolds number $Re = \rho_1 U_m D / \eta$. For the suspensions of 78 μm particles at $U_m \sim 0.6$ m/s we obtain $Re \sim 1500$, corresponding to a laminar flow, while for the suspensions of 467 μm particles at $U_m \sim 2.7$ m/s we obtain $Re \sim 6800$, corresponding to a turbulent flow. Note that in the experiments, the presence of particles in the fluid significantly complicates the flow dynamics with respect to those in pure fluid (Tsuji et al., 1984; Jessop & Jellinek, 2014).

337

The motion of a spherical particle falling through a fluid is controlled by two dimensionless numbers, $\sigma = \rho_2 / \rho_1$ and the particle Reynolds number Re_p . The local flow around the particle may be estimated via $Re_p = \rho_1 dU / \eta$, where $\rho_1 = 1.13$ kg/m³ and $\eta = 1.81 \times 10^{-5}$ kg/(m s) are the density and dynamic viscosity of air, respectively. For the suspension of 78 μm particles, with U_m varying from 0.4 to 0.7 m/s, this gives a $Re_p \sim 1.9$ -3.4. For the suspensions of 467 μm particles, taking $U_m \sim 2.5$ -3 m/s, this gives Re_p ranging from 73-88. The obtained Re_p indicates that all the suspensions studied here are in the transitional flow regime ($1 < Re_p < 1000$) (Rhodes, 2008).

344

345 4.2.2 Effective drag coefficient β

346 Consider a single particle in a suspension and suppose that U_m is equal and op-
 347 posite in direction to its fall velocity. Ignoring fluid inertia, there are three forces act-
 348 ing on the particle, a buoyancy force, a gravitational force and a drag force F_d , so that:
 349 $\pi d^3(\rho_2 - \rho_1)g/6 = F_d$, where $F_d = (1/2)\rho_1 A U_m^2 \beta$, with A the surface of the sphere on
 350 which the drag acts and β the effective drag coefficient. The drag coefficient is calculated
 351 from

$$\beta = dg(4/3)(\rho_2/\rho_1 - 1)/U_m^2 \quad (3)$$

352 and shown as a function of Re_p in Fig. 7b,d. We find that β is a decreasing function of
 353 Re_p similar to the drag coefficient for single particle, C_d , estimated by the Abraham con-
 354 tribution in the transitional flow regime $C_d = [0.5407 + (24/Re_p)^{1/2}]^2$ (Abraham, 1970).
 355 Additionally, we find that for suspensions of small particles, $\beta < C_d$, while for suspen-
 356 sions of larger particles, $\beta > C_d$. This suggests that different mechanisms control the
 357 settling dynamics in suspensions of smaller particles and larger particles, as discussed
 358 below.

359 4.2.3 Hindered settling

360 Particles falling in a particle-laden fluid experience a larger fluid drag than a par-
 361 ticle falling in a pure fluid due to the flow around neighbouring falling particles, an ef-
 362 fect called hindered settling (Richardson & Zaki, 1954; Yin & Koch, 2007; Dey et al.,
 363 2019). Consequently, the mean fall velocity in a homogeneous suspension of spherical
 364 particles is less than the terminal velocity of a single isolated particle. The most widely
 365 used empirical relation between the hindered settling velocity U^* and volumetric par-
 366 ticle concentration ϕ comes from sedimentation and liquid fluidization experiments, which
 367 showed that $U^* = U_t(1 - \phi)^n$ (Richardson & Zaki, 1954), where U_t is the theoretical
 368 settling velocity of a single isolated particle in a pure fluid and n is a power-law expo-
 369 nent that depends on the particle Reynolds number $Re_p(U_t)$. For the range of Re_p in
 370 this study, the relevant hindered settling model includes a prefactor k yielding $U^* = kU_t(1 -$
 371 $\phi)^n$ (Yin & Koch, 2007; Di Felice, 1999) and here $n = 4.4Re_p^{-0.1}$ (Richardson & Zaki,
 372 1954). In order to test such a settling model, the data of U_m and ϕ_{Lm} are compared to
 373 an empirical expression $U_m = p_1(1 - \phi_{Lm})^{p_2}$ which has a similar functional form to
 374 the hindered settling model.

375 For suspensions of 467 μm particles, the data are well described with $p_1 = kU_t =$
 376 2.9 ± 0.1 m/s and $p_2 = 4.89 \pm 2.5$ (Fig. 7c). For a single particle, $U_t \sim 3.5$ m/s, which
 377 implies that $k \sim 0.8$, in agreement with literature values (Yin & Koch, 2007; Di Felice,
 378 1999). Moreover, the exponent obtained from the fit is very close to the improved re-
 379 lationship $n = (5.1 + 0.27 * Re_p^{0.9}) / (1 + 0.1 * Re_p^{0.9})$, where Re_p is calculated from the
 380 theoretical settling velocity of a single particle (Garside & Al-Dibouni, 1977).

381 Hindered settling cannot account for the settling velocity increasing with the solid
 382 volume fraction in suspensions with 78 μm particles. Instead, this dependence may be
 383 captured by power law $U_m = p_3\phi_{Lm}^{p_4} + p_5$, with $p_3 = 2804$ m/s, $p_4 = 1.9 \pm 0.6$. Here
 384 $p_5 = 0.47 \pm 0.02$ m/s represents the single particle settling velocity in the limit of very
 385 low ϕ , which is higher than the predicted theoretical velocity for a single particle $U_t \sim$
 386 0.37 m/s in the intermediate flow regime (Fig. 7a). A power law relation between the
 387 solid volume fraction and the settling velocity was also observed for volcanic ash par-
 388 ticles (Del Bello et al., 2017). On the basis of this comparison, we argue that the set-
 389 tling dynamics in suspensions of small particles is to large extent controlled by the for-
 390 mation of particle clusters as discussed next.

391

4.2.4 Clustering

392

393

394

395

396

397

398

399

400

401

It is difficult to quantify the particle concentration in, and shape of, clusters due to the extensive light scattering by the particles, and the additional problem of interpreting a 2D projection of a 3D structure. Notwithstanding these limitations, the cluster velocity appears to be well defined in the suspensions (Fig. 6 and supplementary movies). Analysis of the cluster trajectories suggests that the mean reduced settling velocity of clusters (i.e., $U_{cluster*}$ in the laboratory reference frame) is slightly lower in suspensions of 78 μm particles than in suspensions of 467 μm particles. However, the cluster velocity for settling in static air is $U_{cluster} = U_{cluster*} + U_m$ yielding $U_{cluster} \sim 0.9+0.7=1.6$ m/s and $U_{cluster} \sim 1.1+2.5=3.6$ m/s in suspension of 78 μm and 467 μm particles, respectively (Fig. 8).

402

403

404

405

406

407

To quantify the contribution of the clusters to the overall settling velocity of the mixture, we evaluate the ratio $U_{cluster}/U_t$. For the suspensions of 78 μm particles we find $U_{cluster}$ is about 4 times larger than U_t , resulting in a significant impact of clusters on the settling dynamics of the suspension (Fig. 8a). Instead, for the 467 μm particles the $U_{cluster} \sim U_t$, making it possible for hindered settling to dominate (which is a settling mechanism for isolated particles) (Fig. 8b).

408

409

410

411

412

413

414

415

416

417

418

419

420

421

422

423

424

The picture that emerges is the following. For suspensions of 78 μm particles, the bulk $Re \sim 1500$ implies a laminar flow. However, spatial fluctuations in the particle concentration may generate turbulence, an effect called cluster induced turbulence (CIT) (Capece de Valcarlos et al., 2015; Fong & Coletti, 2022). CIT occurs when the mass loading $\psi = \sigma\phi/(1-\phi) \gg 1$, which is the case here as $\psi \sim 10$. The elongate and apparently dense clusters have a higher settling velocity than individual particles, resulting in the increase of U_m with ϕ_{Lm} . In contrast, for the suspensions of larger particles, the bulk $Re \sim 6800$ implies turbulent flow. The decrease of U_m with increasing ϕ_{Lm} is well captured by a hindered settling model (Fig. 7c). Significant clustering is also observed in these suspensions, however, as the settling velocity of the clusters is not significantly different than that of a single particle, the clusters do not appear to impact the hindered settling mechanism. In other words, in suspensions of small particles the clusters dominate the settling dynamics, whereas the settling in suspensions of larger particles is dominated by hindered settling. The impact of clusters on particle settling may be related to the different shape, particle concentration, and longevity of the clusters, which in turn may depend on how particles are coupled to fluid motion (Nitsche & Batchelor, 1997; Pignatelli et al., 2011; Chen et al., 2021).

425

426

427

The Stokes number captures the ability of particles to respond to changing flow conditions and is the ratio of the particle response time τ_p to a characteristic flow time scale τ_f (for the largest eddies $\tau_f = D/U_m$), so that

$$\text{St} = \frac{(\rho_2 - \rho_1)d^2U_m}{18\eta D}. \quad (4)$$

428

429

430

431

432

433

434

435

436

437

438

439

Clustering is sensitive to St (Bec, 2003). When $\text{St} \ll 1$ particles are well coupled to the flow and follow streamlines. When $\text{St} \gg 1$ particle motion is decoupled from turbulent motions. When St is of order 1, particles tend to accumulate at the edges of eddies (Maxey, 1987; Bec et al., 2007), leading to a local increase in particle concentration, a process that can initiate cluster formation. Our 78 μm particles at $U_m \sim 0.7$ m/s have $\text{St} = 0.8$, and the $d = 467$ μm particles with $U_m \sim 2.5$ m/s have $\text{St} = 105$ with the above definition of St, meaning that suspensions of smaller particles are more prone to clustering. Clusters of small particles may thus last longer and have higher particle concentrations, and consequently their $U_{cluster}$ and $U_{cluster}/U_m$ are larger than for clusters of high St particles. As a result, clustering may have a dominant role for the smaller particles, while hindered settling prevails for the larger particles. Future experiments and additional probing of particle concentration are needed to disentangle the role of the particle size and

440 the velocity profile on the persistence of clusters as well as cluster shape and concentra-
441 tion.

442 **4.3 Geophysical implications**

443 Our experiments show that the consequence of clusters on the settling velocity de-
444 pends essentially on the Stokes number. Here, relative to the settling velocity of isolated
445 particles U_t , our Stokes number $O(1)$ particles settle with a mean velocity twice as large,
446 and clusters of these particles have settling velocities that are even four times as large.
447 However, our larger Stokes number $O(10^2)$ particles experience hindered settling, with
448 settling speeds up to 30% slower than U_t , while clusters in these suspensions have set-
449 tling velocity roughly equal to U_t . These types of phenomena that arise from 4-way cou-
450 pling are not accounted for in some models of particle transport used to simulate vol-
451 canic plumes, such as Ash3D (Schwaiger et al., 2012), TEPHRA (Bonadonna et al., 2005),
452 FALL3D (Folch et al., 2020) and PLUME-MOM/HYSPLIT (Stein et al., 2015) that con-
453 sider theoretical single-particle settling velocities. Modifications to the particle drag and
454 settling velocity (Fig. 7) translate into additional uncertainty in such models. Settling
455 velocities lower or higher than that of the theoretical velocities for single particles are
456 a possible cause of discrepancy between simulated and observed fall deposit character-
457 istics such as grain size and mass of deposit per unit area (Tadini et al., 2020). As high-
458 lighted in the report by the National Academies of Sciences, Engineering and Medicine
459 (2017), particle-scale processes influence the large scale dynamics of volcanic eruptions.
460 Similarly, in their review of pyroclastic density currents, and relevant to geophysical tur-
461 bulent gas-particles mixtures in general, Lube et al. (2020) wrote “drag law correction
462 and sub-grid models that account for mesoscale clustering must be developed” .

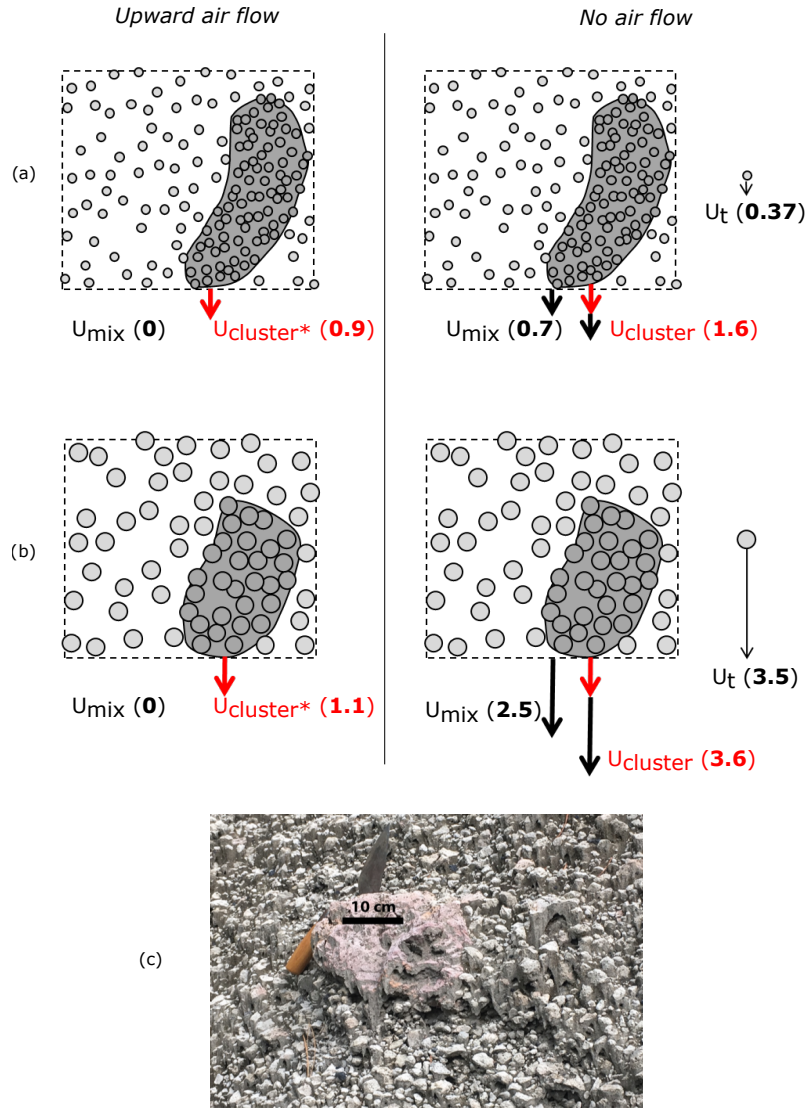


Figure 8. Schematic of the settling velocities (in m/s). (a) Suspensions of $d=78\ \mu\text{m}$ particles. Left panel, settling velocities in the presence of an upward air flow (i.e., velocities in the laboratory reference frame). The mixture is suspended, while clusters settle at a reduced velocity. Right panel, settling in the absence of an air flow. The mixture settles with a velocity $U_{\text{mix}} \sim U_m$ and clusters settle at velocities $\sim U_m + U_{\text{cluster}^*}$. For comparison the terminal settling velocity U_t of a single particle in the intermediate regime is also illustrated. Note that this velocity is significantly less than the settling velocity of the mixture and the clusters. (b) Suspensions of $d=467\ \mu\text{m}$ particles. In this case, the settling velocity of the mixture is less than the theoretical settling velocity of a single particle in the intermediate flow regime. (c) Dacite pumice fall from the 10.5 ka Plinian eruption of Llaima, Chile (Northing 570558, Easting 0271863; photo taken 7 January 2020).

463 One fall deposit characteristic from volcanic plumes that might result from cluster-
 464 ing, and be diagnostic that clustering is an important process in spreading umbrella
 465 clouds, is the occurrence of unusually large clasts in an otherwise well-sorted deposit. As
 466 an illustrative example, we consider the dacite pumice fall from the 10.5 ka Plinian erup-

467 tion of Llaima, Chile (Schindlbeck et al., 2014). Fig. 8c shows unit IIIb of the deposit,
 468 12 km from the vent. Notable is the outsized clast in a matrix of smaller pumice (most
 469 of the deposit consists of cm size lapilli with a small proportion of large clasts). The in-
 470 termediate diameter of the large clast, measured with a ruler, is 16 cm. The median di-
 471 ameter of the pumice, measured by dry sieving in the lab, is 1 cm with an Inman sort-
 472 ing value of 0.45 (see Supplementary Information section 3 for details). 12 km is too dis-
 473 tal for the large clast to be a ballistic bomb. Our hypothesis is that within the spread-
 474 ing umbrella cloud, the lapilli settled in clusters with a similar settling velocity as the
 475 large particle since they were deposited together. We assume that U_m is equal to the fall
 476 velocity of the coarsest particles. For the large and median particle sizes, diameters of
 477 16 and 1 cm respectively, the theoretical settling speeds assuming a density of 600 kg/m^3
 478 are $\sim 61 \text{ m/s}$ and $\sim 14 \text{ m/s}$ using the Abraham (1970) drag model. This implies a roughly
 479 4-fold increase in settling speed for the clusters of small particles, which is similar to the
 480 enhanced settling speed in our experiments (Fig. 8) and mesoclusters in large scale den-
 481 sity current experiments (Breard et al., 2016).

482 More generally in volcanic plumes and spreading umbrella clouds, enhanced (or hindered)
 483 settling can cause deposits with mass per unit area larger (or smaller) and grain
 484 sizes smaller (or larger) than expected for single size particles (Tadini et al., 2020, 2022;
 485 Freret-Lorgeril et al., 2020; Gilchrist & Jellinek, 2021). Clustering in mixtures contain-
 486 ing particles with Stokes number $O(1)$ is an alternative to ash aggregation commonly
 487 assumed in simulations to explain enhanced settling (e.g., Tadini et al., 2022). The fact
 488 that bimodal fallout deposits, such as the one at Llaima (Fig. 8), are relatively rare sug-
 489 gests effective particle size segregation occurs near the vent in most cases. On the other
 490 hand, hindered settling accounts for reduced particle settling velocity, otherwise explained
 491 by non spherical particle shape or the presence of wind (Marchetti et al., 2022). In a broader
 492 context, hindered settling is likely to occur in various types of geophysical flows contain-
 493 ing particles with Stokes number $\gg 1$, and our experiments suggest that this mechanism
 494 can operate at concentrations as low as $\sim 1 \text{ vol.}\%$, which may be surprising.

495 Numerical simulations of pyroclastic currents showed that unrealistically high par-
 496 ticle drag coefficients, at least 30 times larger than commonly estimated for typical vol-
 497 canic particles ($\sim 0.5-1$), were required to match the runout distance of the ash-cloud
 498 surges at Merapi, 2010 (Kelfoun et al., 2017) and Mount Pelée (Martinique), May 8th,
 499 1902 (Gueugneau et al., 2020). To explain the high drag coefficient, Gueugneau et al.
 500 (2020) concluded that hindered settling occurred as a consequence of the increase in par-
 501 ticle concentration towards the lower part of the currents, our experimental findings sup-
 502 port this statement. Even though it is unlikely that hindered settling alone can account
 503 for the large discrepancy between their simulation and the natural case, it may be partly
 504 responsible. Our experiments showing hindered settling provide insights into the pos-
 505 sible settling characteristics of the particles in the basal layer of these natural flows, that
 506 is, with Stokes numbers $\gg 1$ and at concentrations as low as $\sim 1 \text{ vol.}\%$.

507 5 Conclusion

508 We measured the local solid volume fraction in dilute suspensions of glass parti-
 509 cles in air using two independent techniques, acoustic probing and local fluid pressure
 510 measurements. We showed that these techniques yield similar solid volume fractions, thus
 511 providing two attractive tools to investigate optically opaque mixtures in analogue lab-
 512 oratory experiments. We anticipate that a combination of these techniques may be use-
 513 ful if, for example, both the particle concentration and particle size are not known. In-
 514 deed, the local pressure measurements may then be used to obtain a solid volume frac-
 515 tion, which could be used in the sound attenuation calculation to obtain the particle size.

516 Our experiments in a vertical pipe demonstrate that the local particle concentra-
 517 tion in dilute suspensions depends on the initial amount of particles, the particle size,

518 and the air flow velocity. In suspensions of 78 μm particles, higher air velocities were needed
 519 to obtain higher local particle concentrations and we argue this was due to the presence
 520 of clusters that settled faster than individual particles. In contrast, in suspensions of 467
 521 μm particles, higher local particle concentrations were achieved at lower air velocities
 522 as a consequence of hindered settling of the particles, despite the presence of clusters.
 523 Differences in the shape and particle concentration of the clusters may explain their dif-
 524 ferent settling behaviours.

525 Our results have implications for modeling geophysical dilute gas-particle mixtures.
 526 The field example we discuss suggests that in volcanic plumes clusters of relatively small
 527 particles have enhanced settling velocities, similar to that of larger clasts, decreasing the
 528 sorting in fall deposits. Other geophysical flows with particles of broad grain size ranges
 529 are likely to exhibit similar flow dynamics. We conclude that the formation of clusters
 530 and their settling velocities being significantly different than that of single particles should
 531 be considered in models of geophysical processes through drag law corrections.

532 6 Acknowledgement

533 We thank B. Andrews, A. Marshall, B. Brand, G. Giordano, and P. Valdivia for
 534 field sampling, discussions, and ideas about the deposit pictured in Figure 8. We thank
 535 X. Jia for valuable discussions on sound attenuation. This project is part of a program
 536 of the International Research Center of Disaster sciences and sustainable Development
 537 at University Clermont Auvergne. This is Laboratory of Excellence ClerVolc contribu-
 538 tion no XXX. M.M. is supported CIFAR Earth 4D and NSF 2042173.

539 7 Open Research

540 Datasets and a short description for this research are available with DOI: 10.5281/zen-
 541 odo.7565085 on <https://doi.org/10.5281/zenodo.7565085>.

542 References

- 543 Abraham, F. F. (1970). Functional dependence of drag coefficient of a sphere on
 544 reynolds number. *The Physics of Fluids*, *13*, 2194.
- 545 Allegra, J. R., & Hawley, S. A. (1972). Attenuation of sound in suspensions and
 546 emulsions: Theory and experiments. *Journal of the Acoustical Society of*
 547 *America*, *51*, 1545-1564.
- 548 Bagheri, G. H., Bonadonna, C., Manzella, I., & Haas, P. (2013). Dedicated vertical
 549 wind tunnel for the study of sedimentation of non-spherical particles. *Rev. Sci.*
 550 *Instr.*, *84*, 054501.
- 551 Bec, J. (2003). Fractal clustering of inertial particles in random flows. *Physics of*
 552 *Fluids*, *15*, L81.
- 553 Bec, J., Biferale, L., Cencini, M., Lanotte, A., Musacchio, S., & Toschi, F. (2007).
 554 Heavy particle concentration in turbulence at dissipative and inertial scales.
 555 *Physical Review Letters*, *98*, 084502.
- 556 Berruti, F., Pugsley, T. S., Godfroy, L., Chaouki, J., & Patience, G. S. (1995). Hy-
 557 drodynamics of circulating fluidized bed risers: a review. *The Canadian Jour-*
 558 *nal of Chemical Engineering*, *73*, 579-602.
- 559 Bonadonna, C., Philips, J. C., & Houghton, B. F. (2005). Modeling tephra sedimen-
 560 tation from a ruapehu weak plume eruption. *Journal of Geophysical Research*,
 561 *110*, B08209.
- 562 Bonadonna, C., & Phillips, J. C. (2003). Sedimentation from strong volcanic plumes.
 563 *J. Geophys. Res.*, *108*, 2340.
- 564 Brandt, L., & Coletti, F. (2022). Particle-laden turbulence: Progress and perspec-
 565 tives. *Annual Review of Fluid Mechanics*, *54*, 159–189.

- 566 Breard, E. C. P., Lube, G., Jones, J. R., Dufek, J., Cronin, S. J., Valentine, G. A.,
567 & Moebis, A. (2016). Coupling of turbulent and non-turbulent flow regimes
568 within pyroclastic density currents. *Nature Geoscience*, *9*, 767–771.
- 569 Cahyadi, A., Anantharaman, A., Yang, S., Karri, S. R., Findlay, J. G., Cocco, R. A.,
570 & Chew, J. W. (2017). Review of cluster characteristics in circulating fluidized
571 bed (cfb) risers. *Chemical Engineering Science*, *158*, 70-95.
- 572 Capecelatro, J., Desjardins, O., & Fox, R. (2015). On fluid–particle dynamics in
573 fully developed cluster-induced turbulence. *J. Fluid Mech.*, *780*, 578-635.
- 574 Challis, R. E., Povey, M. J. W., Mather, M. J., & Holmes, A. K. (2005). Ultra-
575 sound techniques for characterizing colloidal disperions. *Reports on progress in*
576 *physics*, *68*, 1514-1637.
- 577 Chen, P., Chen, S., Yang, M., & Li, S. (2021). Falling clouds of particles with finite
578 inertia in viscous flows. *Physics of Fluids*, *33*, 033314.
- 579 Del Bello, E., Taddeucci, J., de' Michieli Vitturi, M., Scarlato, P., Andronico, D.,
580 Scollo, S., ... Ricci, T. (2017). Effect of particle volume fraction on the set-
581 tling velocity of volcanic ash particles: Insights from joint experimental and
582 numerical simulations. *Scientific Reports*, *7*, 39620.
- 583 Dey, S., SK, A. Z., & E., P. (2019). Terminal fall velocity: the legacy of stokes from
584 the perspective of fluvial hydraulics. *Proc. R. Soc. A*, *475*, 20190277.
- 585 Di Felice, R. (1999). The sedimentation velocity of dilute suspensions of nearly
586 monosized spheres. *Int. J. Multiphase Flow*, *25*, 559.
- 587 Epstein, P. S., & Carhart, R. R. (1953). The absorption of sound in suspensions and
588 emulsions. i. waterfog in air. *Journal of the Acoustical Society of America*, *25*,
589 553-565.
- 590 Folch, A., Mingari, L., Gutierrez, N., Hanzich, M., Macedonio, G., & Costa, A.
591 (2020). Fall3d-8.0: a computational model for atmospheric transport and de-
592 position of particles, aerosols and radionuclides – part 1: Model physics and
593 numerics. *Geoscientific Model Development*, *13*, 1431–1458.
- 594 Fong, K. O., & Coletti, F. (2022). Experimental analysis of particle clustering in
595 moderately dense gas-solid flow. *J. Fluid Mech.*, *933*, A6.
- 596 Fornari, W., Picano, F., Sardina, G., & Brandt, L. (2016). Reduced particle settling
597 speed in turbulence. *J. Fluid Mech.*, *808*, 153-167.
- 598 Fornari, W., Zade, S., Brandt, L., & Picano, F. (2019). Settling of finite-size parti-
599 cles in turbulence at different volume fractions. *Acta Mech*, *230*, 413-430.
- 600 Freret-Lorgeril, V., Gilchrist, J., Donnadieu, F., Jellinek, A. M., Delanoë, J.,
601 Latchimy, T., ... S., V. (2020). Ash sedimentation by fingering and sed-
602 iment thermals from wind-affected volcanic plumes. *Earth and Planetary*
603 *Science Letters*, *534*, 116072.
- 604 Fullmer, W. D., & Hrenya, C. M. (2017). The clustering instability in rapid granular
605 and gas-solid flows. *Annual review of fluid mechanics*, *49*, 485-510.
- 606 Garside, J., & Al-Dibouni, M. R. (1977). Velocity-voidage relationships for flu-
607 idization and sedimentation in solid-liquid systems. *Ind.Eng Chem. Proc. Des.*
608 *Dev.*, *16*, 206-214.
- 609 Gilchrist, J. T., & Jellinek, A. M. (2021). Sediment waves and the gravitational sta-
610 bility of volcanic jets. *Bull Volcanol*, *83*, 64.
- 611 Gueugneau, V., Kelfoun, K., Charbonnier, S., Germa, A., & Carazzo, G. (2020).
612 Dynamics and impacts of the may 8th, 1902 pyroclastic current at mount
613 pelée (martinique): New insights from numerical modeling. *Frontiers in Earth*
614 *Science*, *8*, 279.
- 615 Jessop, D. E., & Jellinek, A. M. (2014). Effects of particle mixtures and nozzle
616 geometry on entrainment into volcanic jets. *Geophysical Research Letters*, *14*,
617 060059.
- 618 Kelfoun, K., Gueugneau, V., Komorowski, J. C., Aisyah, N., Cholikh, N., & Mer-
619 ciecca, C. (2017). Simulation of block-and-ash flows and ash-cloud surges
620 of the 2010 eruption of merapi volcano with a two-layer model. *Journal of*

- 621 *Geophysical Research: Solid Earth*, *122*, 4277–4292.
- 622 Lube, G., Breard, E., Esposti-Ongaro, T., Dufek, J., & Brand, B. (2020). Multi-
623 phase flow behaviour and hazard prediction of pyroclastic density currents.
624 *Nature Reviews Earth & Environment*, *1*, 348–365.
- 625 Marchetti, E., Poggi, P., Delle Donne, M., D. and Pistolesi, Bonadonna, C., Bagheri,
626 G., Pollastri, S., . . . Ripepe, M. (2022). Real-time tephra-fallout accumu-
627 lation rates and grain-size distributions using asher (ash collector and sizer)
628 disdrometers. *Journal of Volcanology and Geothermal Research*, *429*, 107611.
- 629 Maxey, M. R. (1987). The gravitational settling of aerosol particles in homogeneous
630 turbulence and random flow fields. *Journal of Fluid Mechanics*, *174*, 441-465.
- 631 National Academies of Sciences, Engineering and Medicine. (2017). *Volcanic erup-*
632 *tions and their repose, unrest, precursors, and timing*. Washington DC: The
633 National Academies Press.
- 634 Nielsen, P. (1993). Turbulence effects on the settling of suspended particles. *J. Sedi-*
635 *ment. Petrol*, *63*, 835-838.
- 636 Nitsche, J. M., & Batchelor, G. K. (1997). Break-up of a falling drop containing dis-
637 persed particles. *J. Fluid Mech.*, *340*, 161-175.
- 638 Pierce, A. D., Siegmann, W. L., & Brown, E. (2016). Suspension theory for the
639 effect of silt particles on attenuation of the compressional waves in marine mud
640 sediments. *Proc. Mtgs. Acoust.*, *29*, 005003.
- 641 Pignatel, F., Nicolas, M., & Guazzelli, E. (2011). A falling cloud of particles at a
642 small but finite reynolds number. *J. Fluid Mech.*, *671*, 34-51.
- 643 Rhodes, M. (2008). *Introduction to particle technology, second edition*. West Sussex,
644 England: John Wiley & Sons, Ltd.
- 645 Richardson, J. F., & Zaki, W. N. (1954). Sedimentation and fluidisation, part i.
646 *Trans. Inst. Chem. Eng.*, *32*, 35-53.
- 647 Schindlbeck, J. C., Freundt, A., & Kutterolf, S. (2014). Major changes in the
648 post-glacial evolution of magmatic compositions and pre-eruptive conditions of
649 llaima volcano, andean southern volcanic zone, chile. *Bulletin of Volcanology*,
650 *76*, 830.
- 651 Schwaiger, H. F., Denlinger, R. P., & Mastin, L. G. (2012). Ash3d: A finite-volume,
652 conservative numerical model for ash transport and tephra deposition. *Journal*
653 *of Geophysical Research*, *117*, B04204.
- 654 Steger, C. (1998). An unbiased detector of curvilinear structures. *EEE Trans. Pat-*
655 *tern Anal. Mach. Intell.*, *20*, 113-125.
- 656 Stein, R. R., A. F. and Draxler, Rolph, G. D., Stunder, B., Cohen, M. D., & Ngan,
657 F. (2015). Noaa’s hysplit atmospheric transport and dispersion modeling
658 system. *Bulletin of the American Meteorological Society*, *96*, 2059-2078.
- 659 Tadini, A., Gouhier, M., Donnadiu, F., de’ Michieli Vitturi, M., & Pardini, F.
660 (2022). Particle sedimentation in numerical modelling: A case study from the
661 puyehue-cordón caulle 2011 eruption with the plume-mom/hysplit models.
662 *Atmosphere*, *13*, 784.
- 663 Tadini, A., Roche, O., Samaniego, P., Guillin, A., Azzaoui, N., Gouhier, M., . . .
664 Le Penneç, J. L. (2020). Quantifying the uncertainty of a coupled plume and
665 tephra dispersal model: Plume-mom/hysplit simulations applied to andean
666 volcanoes. *Journal of Geophysical Research*, *125*, 1-20.
- 667 Tsuji, Y., Morikawa, Y., & Hiroshi, S. (1984). Ldv measurements of an air-solid two-
668 phase flow in a vertical pipe. *J. Fluid Mech.*, *139*, 417-434.
- 669 Uhlmann, M., & Doychev, T. (2014). Sedimentation of a dilute suspension of
670 rigid spheres at intermediate galileo numbers: the effect of clustering upon the
671 particle motion. *J. Fluid Mech.*, *752*, 310-348.
- 672 Urlick, R. J. (1948). The absorption of sound in suspensions of irregular particles.
673 *Journal of the Acoustical Society of America*, *20*, 283-288.
- 674 van den Wildenberg, S., Jia, X., & Roche, O. (2020). Acoustic probing of the par-
675 ticle concentration in turbulent granular suspensions in air. *Scientific Reports*,

- 676 10, 16544.
677 Wang, L. P., & Maxey, M. R. (1993). Settling velocity and concentration distri-
678 bution of heavy particles in homogeneous isotropic turbulence. *J. Fluid Mech.*,
679 256, 27-68.
680 Weit, A., Roche, O., Dubois, T., & Manga, M. (2019). Maximum solid phase con-
681 centration in geophysical turbulent gas-particle flows: Insights from laboratory
682 experiments. *Geophysical Research Letters*, 46, 6388-6396.
683 Yin, X., & Koch, D. L. (2007). Hindered settling velocity and microstructure in sus-
684 pensions of solid spheres with moderate reynolds numbers. *Phys. Fluids*, 19,
685 093302.
686 Ying, C. F., & Truell, R. (1956). Scattering of a plane longitudinal wave by a spher-
687 ical obstacle in an isotropically elastic solid. *Journal of applied physics*, 27,
688 1086-1097.